J. Fluid Mech. (2000), *vol.* 410, *pp.* 211–233. Printed in the United Kingdom

Microgravity experiments and analysis of oscillatory thermocapillary flows in cylindrical containers

By Y. KAMOTANI, S. OSTRACH AND J. MASUD†

Department of Mechanical and Aerospace Engineering, Case Western Reserve University, Cleveland, Ohio 44106-7222, USA

(Received 13 January 1999 and in revised form 21 October 1999)

Results are reported of thermocapillary flow experiments performed aboard the Spacelab. Oscillatory thermocapillary flows were investigated in open cylindrical containers filled with 2 cS kinematic viscosity (Prandtl number = 27 at 25 °C) silicone oil. The fluid was heated by a cylindrical cartridge heater placed at the symmetry axis of the container while the container sidewall was maintained at a lower temperature. Test containers with three different diameters of 1.2, 2.0 and 3.0 cm were used. The ratio of heater to test container diameter was fixed at 0.1. The liquid free-surface shape was either flat or concave. The flow and temperature fields were investigated for steady and oscillatory flows. Free-surface deformation was observed during oscillations. The conditions for the onset of oscillatory flow were determined. It is shown that the Marangoni number alone does not correlate the onset conditions. A new parameter, which represents free surface deformation, is derived for flat free surfaces and is shown to correlate the onset conditions well. Infrared images of free surface and oscillation frequencies are also presented.

1. Introduction

Thermocapillary flow is driven by temperature-induced surface tension variations along a liquid free surface. It is known to become oscillatory under certain conditions. Lately many researchers have given attention to various aspects of steady and oscillatory thermocapillary flows. They have been investigated, theoretically as well as experimentally, under various configurations (thin liquid layers and floating zones), for high, low and unit-order Prandtl number (Pr) fluids, and with negligible and non-negligible buoyancy. The focus of the present work is on oscillatory thermocapillary flows of high-Pr fluids in containers of unit-order aspect ratio with negligible buoyancy, because the subject is uniquely different from other situations, as described below. Most of the past experiments on oscillatory thermocapillary flow in containers of unit-order aspect ratio have been conducted in the so-called floating-zone configuration in normal gravity and some microgravity data are also available (see, for example, Preisser, Schwabe & Scharmann 1983; Velten, Schwabe & Scharmann 1991; Masud, Kamotani & Ostrach 1997). We have investigated steady thermocapillary flows in open unit-order-aspect-ratio cylindrical containers in microgravity

† Present Address: PAF College of Aeronautical Engineering, National University of Sciences and Technology, Pakistan.

(Kamotani, Ostrach & Pline 1994, 1995) and also oscillatory flows in the same configuration in normal gravity (Kamotani *et al.* 1992; Kamotani, Masud & Pline 1996*b*).

Despite all these investigations the cause of time-periodic oscillations in containers of unit-order aspect ratio is not yet fully understood. One important question remains concerning the role of free surface deformation in the oscillation mechanism for high Prandtl number fluids. Some theoretical studies are available in which the oscillation phenomenon is treated as a type of hydrodynamic instability without involving free surface deformation and they predict critical Marangoni numbers for the instability (e.g. Wanschura *et al.* 1995). However, available experimental data for high-*Pr* fluids do not support the existence of critical Marangoni numbers (e.g. Masud *et al.* 1997). In the case of containers of unit-order aspect ratio filled with high-*Pr* fluids, when the Marangoni number becomes sufficiently large, the thermocapillary driving force becomes concentrated in the regions near the hot and cold walls, called hot and cold corners. We have shown that the oscillation phenomenon is closely associated with the hot corner flow. For that reason, the cause of oscillatory thermocapillary flows of high-*Pr* fluids in containers of unit-order aspect ratio is uniquely different. Since experiments in normal gravity tend to be influenced by buoyancy to various degrees, more microgravity experiments covering wider parametric ranges are needed to complete our understanding. For that reason we have performed experiments on oscillatory thermocapillary flows, called the Surface Tension Driven Convection Experiment-2 (STDCE-2), aboard the USML-2 Spacelab in 1995. In STDCE-2, steady and oscillatory thermocapillary flows were generated in open cylindrical containers. Two types of heating modes were employed: external heating by a laser beam and internal heating by a submerged heater. Some of the results from the laser heating experiments have been presented in Kamotani, Ostrach & Masud (1998). The data taken in the submerged heating mode are presented herein. The oscillatory flow structures and the conditions for the onset of oscillations are presented. In addition, the physical mechanism of oscillations is described and, based on the model, a surface deformation parameter is derived.

2. Experimental description, conditions, and procedure

2.1. *Description*

A detailed description of the hardware involved in the STDCE-2 experiments is given by Pline *et al.* (1996), so only some important features of the experimental setup are discussed herein. The experimental arrangement is shown in figure 1. Three cylindrical containers with copper sidewalls having $D = 1.2$, 2.0 and 3.0 cm inner diameters were used. Container depth was fixed at one half of the container diameter. The bottom of the container was made of Teflon. Water from a heat exchanger cooled the outer wall of the test container in order to maintain the container wall at a uniform temperature. The sidewall temperature was about 14 °C. A cylindrical electrical resistance heater was placed along the centreline of the test container; its diameter was fixed at 10% of the container diameter. The top of the heater was flat and aligned with the top edge of the container side wall. Silicone oil with kinematic viscosity of 2 cS manufactured by Dow Corning was the test fluid. The properties of the fluid were supplied by the company. The static free surface shape of the test was variable. Figure 2 shows the shapes investigated in STDCE-2, one flat and two concave, which were obtained by adjusting the total amount of fluid in the container. The test fluid was in contact with air.

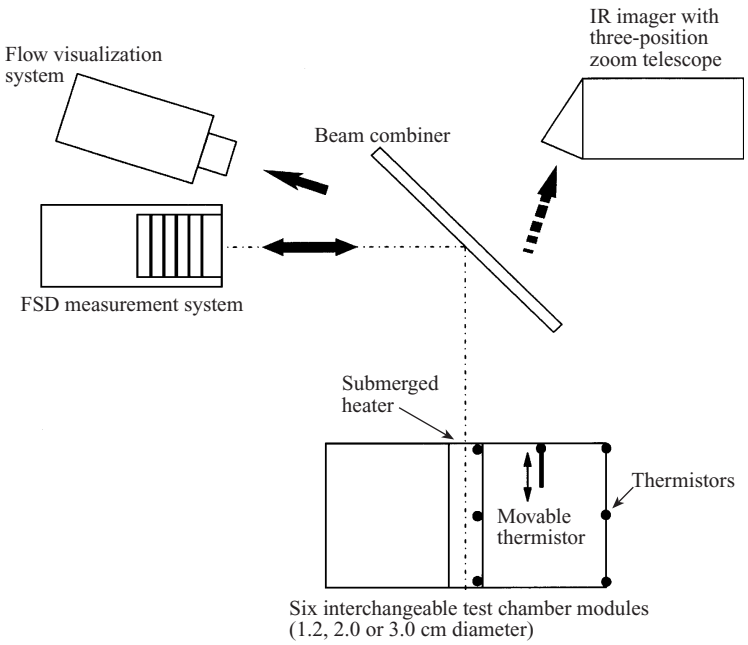

FIGURE 1. Experimental arrangement.

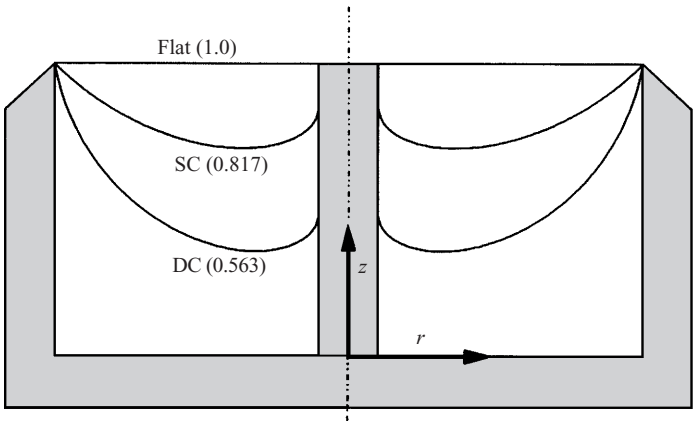

FIGURE 2. Free surface shapes tested in STDCE-2. The curved surface shapes are computed numerically. The number within parentheses for each shape is the total fluid volume relative to that for flat surface. SC = shallow concave, DC = deep concave.

Flow was visualized by mixing Pliolite particles of about 70 μm size into the test fluid as tracer particles and observing the whole flow field through a CCD camera placed above the test section (see figure 1). A laser diode light source was used for illuminating the flow field. An infrared scanner (IR imager) was used to measure the thermal radiation from the free surface in the wavelength range between 8 and 14 μm. The imager was identical to that used in our previous Space experiments and its description is given by Pline & Butcher (1990). A zoom telescope was fitted to the imager in the STDCE-2 design to properly magnify the three test cell sizes. The free surface temperature fields were constructed from the IR images by using THERMAGRAM95 software. The sensitivity of the imager is about 0.2 °C and the spatial

resolution is about 2% of the chamber diameter. Radiation absorption length of the test fluid in the above wavelength range is 0.02 mm (Pline 1988).

An optical system based on the Ronchi test was used for measuring free surface deformations. The principle of the Ronchi test is described by Malacara (1992): it was performed by observing the shadow pattern produced when a focused beam was passed through a grating. A Ronchigram was obtained by superimposing the shadow pattern upon an image of the surface. Information about the surface was obtained by correlating shadow lines with physical locations on the surface. The slopes of the surface at various locations were determined. The free surface shape was constructed from the slope information by integration. The Ronchi system used in the STDCE-2 is described in detail by Stahl & Stultz (1997). Various gratings were used to cover a range of surface slope from 5 to 30 μm mm^{-1}. The Ronchi measurements were made only in the flat surface tests.

Three thermistors were imbedded inside each of the heater and the container wall, as shown in figure 1. Since the thermistors were imbedded inside the heater shell and at some distance away from the liquid free surface (pinning edge at the top of the heater), the heater temperature based on this measurement was generally higher than the heater surface temperature near the pinning edge. In order to compensate for this, a ground-based calibration was done for all the test containers to relate the heater thermistor output to the actual temperature at the heater top edge. One thermistor probe measured the liquid temperature. This probe was located at the mid-radial location (see figure 1) and its axial position was controlled manually. The probe was withdrawn to the bottom plate during the determination of onset of oscillations to avoid its interference. In addition, one thermistor measured the ambient air temperature above the test fluid.

The video pictures from flow visualization, the IR imager and the Ronchi system were recorded on-board as well as downlinked in real time for the investigators on the ground. The data from the thermistors was downlinked at a rate of 1 Hz and was recorded on-board at a rate of 10 Hz.

2.2. *Ranges of parameters*

The relevant dimensionless parameters for steady thermocapillary flow in the present configuration, with negligible gravity and non-deformable free surface, are Marangoni number $Ma = \sigma_T \Delta T R/\mu\alpha$, Prandtl number $Pr = \nu/\alpha$, aspect ratio $A = H/R$, and heater ratio $H_r = R_h/R$, where ΔT is the temperature difference between the heater and the sidewall, R is the container radius, H is the depth, R_h is the heater radius, μ is the fluid dynamic viscosity, ν is the kinematic viscosity, α is the fluid thermal diffusivity, and σ_T is the temperature coefficient of surface tension. The Reynolds number of the flow, R_σ, can be computed as Ma/Pr. In the case of curved free surface tests, one needs to specify also the static free surface shapes. Based on the numerical analysis to be discussed later, heat loss from the free surface due to radiation and forced convection is less than 5% of total heat transfer rate, so it is not important in the present experiments.

A and H_r were fixed at 1.0 and 0.1, respectively, in STDCE-2; and $Pr = 33$ and $Ma < 6 \times 10^5$. The fluid viscosity varied by as much as 40% from the sidewall temperature (T_c) to the heater temperature (T_h) in the STDCE-2 flat surface tests. As will be shown later, the temperature of bulk fluid is near T_c, so that the viscosity used in calculating Pr and Ma is evaluated at T_c. A total of five tests were performed with flat free surfaces. Two concave shapes were investigated, which are referred to as shallow and deep concave shapes herein. The concave shapes shown in figure 2

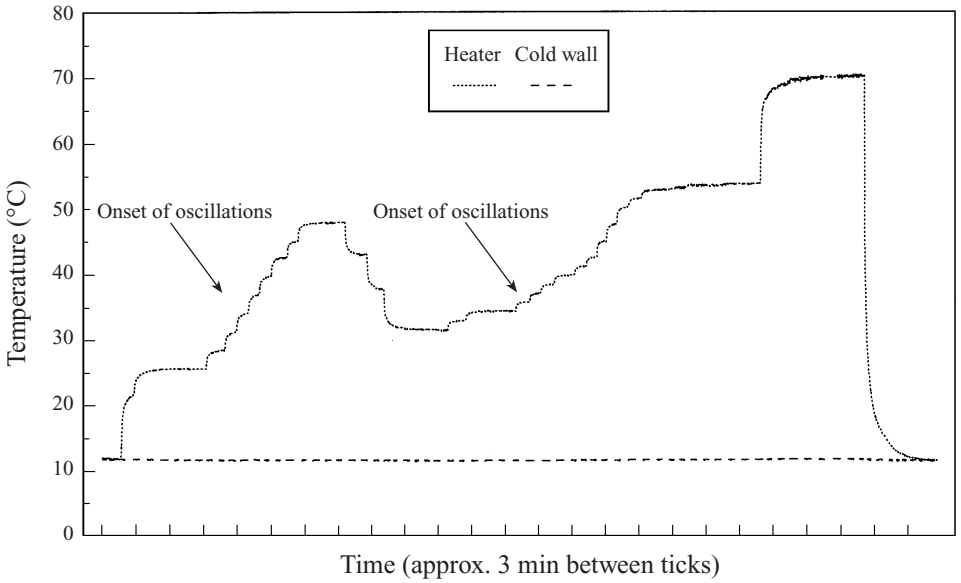

FIGURE 3. General time line of tests conducted during STDCE-2. The figure shows how the heater and cold wall temperatures are varied in a typical test.

are obtained by solving a meniscus equation describing uniform capillary pressure along the free surface for a given total fluid volume. The total volume relative to that for flat surface, the relative fluid volume V_r, is given in figure 2. The free surface is pinned at the top edge of the sidewall. The contact angle at the heater surface is set at 5°, based on our observation. Eight tests were performed with concave surfaces.

2.3. *Procedure*

Generally, we utilized the following procedure in the STDCE-2 tests. First, the appropriate test container module was installed in the experimental rack after shaking gently to disperse the tracer particles in the fluid kept in a reservoir. Then, the test container was filled from the reservoir until a flat free surface was achieved (judged by the Ronchi system to within 0.1 mm). In a curved free surface test, a specified amount of fluid was withdrawn from the flat surface location. The final curved surface shape was checked by positioning the movable thermistor probe close to the free surface. The final curved shapes were within $\pm 5\%$ of the specified shapes in figure 2. At this time the operations were paused to allow the hardware and test container/fluid to reach thermal equilibrium (noted from various temperature outputs). Then the experiment was started by energizing the heater and monitoring the flow field and temperature outputs to identify steady flow. A typical time sequence is shown in figure 3. The initial heater power level was set at a value below the onset of oscillations. Then, the heater power was increased in small steps with adequate time between the steps to allow the flow to reach steady state. After the transition to oscillatory flow was identified, the heater power was reduced to achieve steady flow again and then increased in smaller steps until oscillatory flow was observed again. Once the onset of oscillations was identified, the heater power was further increased to study the oscillatory flow phenomena. Three video images (flow visualization, IR and Ronchi data) were downlinked in real time to the ground station where we monitored the STDCE-2 tests. The onset of oscillations was identified by detecting small but

systematic changes in the video images. Several trained scientists participated in the identification task. After the flight, the task was made much easier by examining those videotapes in fast-forward mode, which showed that the onset occurred almost simultaneously in all three images.

2.4. *Experimental accuracy*

The temperature non-uniformity along the heater wall and the test container wall was within $\pm 3\%$. The thermistors employed in the STDCE-2 tests had an accuracy of $\pm 0.1\,^{\circ}\mathrm{C}$ and a response time of 0.1 s. The uncertainty in determining the onset of oscillations was estimated to be $\pm 2\,^{\circ}\mathrm{C}$ for the 1.2 cm, $\pm 1.3\,^{\circ}\mathrm{C}$ for the 2.0 cm, and $\pm 1.4\,^{\circ}\mathrm{C}$ for the 3.0 cm diameter test container. This uncertainty was due to the heater power increment just before the onset of oscillations.

3. Numerical analysis

In addition to the experiments, a numerical analysis is performed to study the basic steady flow fields. The numerical schemes for both flat and curved free surfaces have been validated in our past work (Kamotani *et al.* 1994, 1995). For this steady analysis, the free surface is assumed to be non-deformable, since the range of capillary number in STDCE-2 as well as in our ground-based work is much less than unity. Fluid viscosity and surface tension vary with temperature. The bottom wall is assumed to be thermally insulating. Radiative and convective heat loss from the free surface is taken into account in the analysis. The velocity and stream function are non-dimensionalized by $\sigma_T \Delta T/\mu$ and $\sigma_T \Delta T R^2/\mu$, respectively, and the temperature is non-dimensionalized as $(T - T_c)/\Delta T$. The cylindrical coordinate system used in the present work is shown in figure 1.

The scheme for flat surface is based on the SIMPLER algorithm. A non-uniform grid system is employed with meshes graded towards the heater and container walls in the r-direction and towards the free surface in the z-direction. At $Ma = 1.2 \times 10^5$ (near the largest value for the steady flow), the values of maximum dimensionless stream function computed with three different grids, 46×40 ($r \times z$), 58×51, and 80×60 with the smallest radial mesh sizes next to the heater of 0.001, 0.0005, and 0.0002, respectively, are 9.11×10^{-4}, 9.17×10^{-4}, and 9.17×10^{-4}. The values of dimensionless heat transfer rate, Nusselt number, are 4.92, 4.91, and 4.90, respectively. Therefore, the 58×51 grid system is used in the present flat surface analysis.

The numerical scheme for curved free surface is described by Kamotani & Platt (1992). The grid system is similar to the one used for the flat surface. Based on similar grid-dependence studies as above, a 58×51 grid system with the smallest radial mesh size of 0.002 and a 67×60 grid system with the smallest mesh of 0.002 are employed for the shallow and the deep concave surface, respectively.

4. Analysis of basic steady flow

The basic flow field with a flat free surface is analysed first. A set of typical computed streamlines and isotherms for steady flow in a fixed radial (r, z)-plane is presented in figure 4. The flow field is unicellular (called the flow cell herein) with rapid outward flow from the heater to the cold wall along the free surface (the surface flow) and a return flow towards the heater in the bulk (the return flow). Convection due to the unicellular motion causes thin thermal boundary layers along the free surface and near the heater. Large temperature drops occur across those boundary layers so

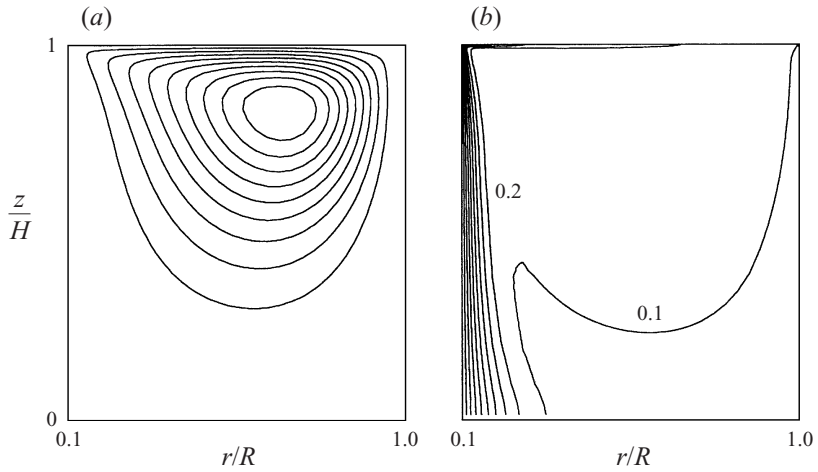

FIGURE 4. Typical streamlines (*a*) and isotherms (*b*) for steady flow with flat free surface ($Ma = 1.3 \times 10^5$, $Pr = 30$, $H_r = 0.1$, and $A = 1$). The dimensionless maximum stream function is equal to 9.7×10^{-4}.

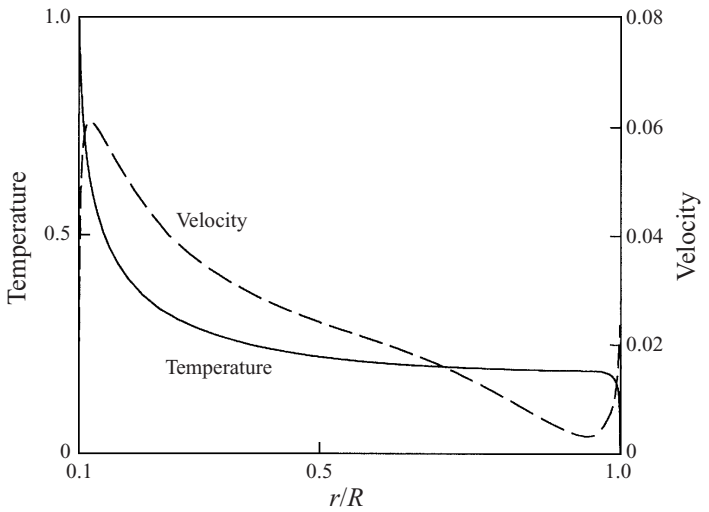

FIGURE 5. Computed surface velocity and surface temperature distributions for the conditions of figure 4.

that most of the fluid remains relatively cool. The computed surface temperature and velocity distributions are shown in figure 5 for the conditions of figure 4. Because of the thin thermal boundary layer along the free surface, the surface temperature exhibits a large radial temperature gradient in the region close to the heater, and, as a result, the surface velocity is relatively large in that region. In the following discussion the flow field is divided into two: the region near the liquid–heater contact line where the radial temperature gradient and velocity are large, called the hot corner; and the rest of the container, called the bulk region.

Kamotani, Chang & Ostrach (1996*a*) studied the steady flow field in the present configuration by numerical and scaling analyses in the parametric range where the overall flow is mainly due to the driving force in the hot corner. However, as will

be discussed later, a velocity boundary layer appears along a certain portion of the free surface, including the hot corner, when R_σ becomes sufficiently large. Then, the mass flux out of the hot corner, being confined to the thin boundary layer, becomes relatively small compared to that of the bulk flow, so the thermocapillary driving force in the hot corner becomes less important for the overall flow. Oscillations are found in the parametric range where the thermocapillary force in the bulk region drives the overall flow. Various velocity and length scales are derived below for that situation by scaling analysis, as they are needed in the later data analysis. A and H_r are considered fixed in the following analysis, for simplicity, so that only one length scale (R) is used.

The bulk region is analysed first. The concentrated heat flux coming out of the hot corner forms a thermal boundary layer along the free surface (similar to a thermal jet). The total heat transfer rate (Q) scales with the amount of convection through the boundary layer,

$$Q \sim \rho C_p U_0 \Delta T_b \delta_{TS} R \sim \rho C_p \Delta T_b (\alpha R U_0)^{1/2} R, \tag{4.1}$$

where U_0 is the characteristic bulk velocity, ΔT_b is the characteristic temperature variation in the bulk region, ρ is the fluid density, and C_p is the fluid specific heat; δ_{TS} is the thermal boundary layer thickness and estimated as $\delta_{TS} \sim (\alpha R/U_0)^{1/2}$, where α is the thermal diffusivity of the fluid. The z-location of the centre of the flow cell is 0.81 in figure 4 (for $Ma = 1.3 \times 10^5$). In our earlier work it was shown that the cell centre location was 0.79 for $Ma = 300$ (Kamotani *et al.* 1996*a*). The fact that the z-location of the cell centre is nearly unchanged over such a wide range of Ma shows that the bulk flow is viscous dominated. Therefore, velocity scale U_0 can be determined from the shear stress balance at the free surface, which gives, for a fixed A,

$$U_0 \sim \frac{\sigma_T \Delta T_b}{\mu}. \tag{4.2}$$

The total flow rate in the container or the maximum stream function, ψ_{max}, is mainly determined by the bulk flow so that $\psi_{max} \sim U_0 R^2$. Using (4.1) and (4.2), ψ_{max} can be expressed as

$$\frac{\psi_{max}}{\alpha R} \sim \left(\frac{\sigma_T Q}{k\mu\alpha}\right)^{2/3}, \tag{4.3}$$

where k is the fluid thermal conductivity. From (4.1) and (4.2) the Marangoni number for the bulk flow (Ma_b), which is based on ΔT_b and R, can be derived as

$$Ma_b \equiv \frac{\sigma_T \Delta T_b R}{\mu\alpha} = \left(\frac{\sigma_T Q}{k\mu\alpha}\right)^{2/3}. \tag{4.4}$$

Therefore, (4.3) is a viscous scaling law showing proportionality between the dimensionless total flow rate and the bulk Marangoni number. The scaling law is compared with the results from the numerical analysis for three values of Pr in figure 6. In this numerical analysis, the fluid viscosity is assumed to be invariant with temperature so as to be consistent with the scaling analysis. As seen in the figure, there is very good agreement in the range $Ma_b > 200$. Also, the computed results do not depend on Pr, which shows that the bulk flow is mainly viscous dominated.

The total heat flux Q was measured in the laser heating mode, but the temperature difference ΔT, instead of Q, was measured in the submerged heater mode. In order to relate Q in the above analysis to ΔT, one must analyse the flow and temperature fields near the heater including the hot corner. We have analysed the same region

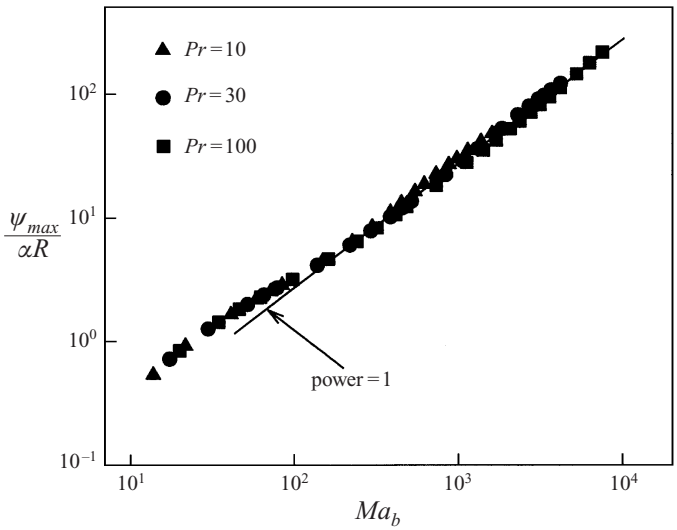

FIGURE 6. Scaling law for bulk flow: maximum stream function versus bulk Marangoni number.

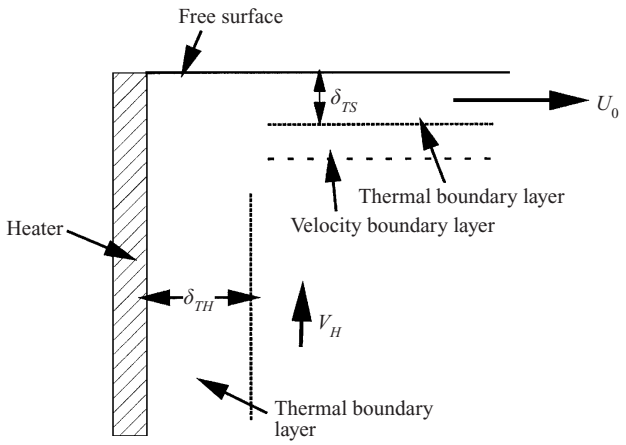

FIGURE 7. Sketch of the hot corner near the heater.

for the floating-zone configuration (Kamotani & Ostrach 1998). The present and floating-zone (FZ) configurations are similar in that they have heating and cooling walls with ΔT imposed across them. However, there is an important difference in that the overall flow is mainly driven in the hot corner in the FZ configuration but it is driven in the bulk region in the present configuration.

The flow field near the hot corner is sketched in figure 7. A large surface temperature gradient exists near the heater because of the thermal boundary layer along the heater, so the extent of the hot corner is characterized by the thermal boundary layer thickness along the heater, δ_{TH}. Since the overall flow is mainly driven in the bulk region, the velocity scale in the hot corner is the same as in the bulk region, namely U_0. As discussed by Kamotani *et al.* (1996*a*), inertia forces begin to affect the flow, starting from the hot corner, in the range $R_\sigma > 2000$, so a velocity boundary layer exists along a certain portion of the free surface in the present parametric range. However, since most of the bulk flow is still viscous dominated, as discussed earlier, the overall

effect of inertia forces is not large. For that reason, the primary parameter is still Ma. When the velocity boundary layer appears around R_σ of 2000, its interaction with the bulk flow is different for different Pr fluids because Ma and thus the bulk flow are different at that R_σ. Therefore, we assume Pr is fixed in the present analysis for simplicity.

As mentioned above, a velocity boundary layer exists along a certain portion of the free surface. The boundary layer entrains the surrounding fluid as it develops, and the entrainment velocity determines the fluid velocity along the heater, V_H, as sketched in figure 7. As such, V_H is much smaller than the velocity scale in the boundary layer direction, namely U_0. Based on the numerical analysis, the radial extent of this low-velocity region from the heater ranges roughly from 0.1 to 0.2 in the present parametric range. For a given Pr, the velocity boundary layer thickness is considered to scale with the thermal boundary layer thickness along the free surface, δ_{TS}. Then, one can balance the volume flux within that slow moving region along the heater and the volume flux in the boundary layer, namely

$$V_H \sim U_0 \, \delta_{TS} / R \tag{4.5}$$

for a given Pr. Then, the thickness of boundary layer along the heater can be estimated as

$$\delta_{TH} \sim (\alpha R / V_H)^{1/2}. \tag{4.6}$$

The total heat transfer rate from the hcater scale as $Q \sim k \Delta T R_h R / \delta_{TH}$ and it can be shown that the total conduction heat transfer rate is $k \Delta T R / (-\ln H_r)$, so the Nusselt number, which is the ratio of the above two heat fluxes, can be estimated, for a given H_r, as

$$Nu \sim R / \delta_{TH}. \tag{4.7}$$

From (4.1)–(4.7) one obtains the following scaling laws in terms of Ma for a given A, H_r and Pr:

$$\left.\begin{aligned} &Nu \sim Ma^{1/5}, \quad Ma_b \sim Ma^{4/5}, \quad \delta_{TS}/R \sim Ma^{-2/5}, \\ &\mu U_0 / \sigma_T \Delta T \sim Ma^{-1/5}, \quad \mu V_H / \sigma_T \Delta T \sim Ma^{-3/5}. \end{aligned}\right\} \tag{4.8}$$

The first two scaling laws can be directly compared with the numerical results, which is done in figure 8. The figure shows that although the numerical results, especially for Nu, depend slightly on Pr for a given Ma due to non-negligible inertia forces, they agree reasonably well with the scaling laws for a given Pr in the range where $R_\sigma (= Ma/Pr)$ is larger than about 2000. The scaling law for Ma_b in (4.8) gives us the relation between Q and ΔT. Those scaling laws will be used in the later analysis.

Typical streamlines and isotherms for the deep concave free surface are shown in figure 9. The flow and temperature fields are qualitatively similar to those for the flat surface. The unicellular structure agrees well with the observed pattern. As discussed by Kamotani & Platt (1992), the flow with the concave free surface tends to be slower than that with the flat surface, for two reasons. One is that the average flow passage is narrower and the other is that the direction of the thermocapillary force varies along the free surface, which makes it less effective in driving the flow cell. The computed maximum stream function, which represents the overall flow rate, is shown as a function of Ma in figure 10 for three surface shapes. The maximum value of Ma in each case is close to the maximum Ma at which the flow was found to be steady in STDCE-2. As seen in figure 10, the value of ψ_{max} decreases when the surface becomes

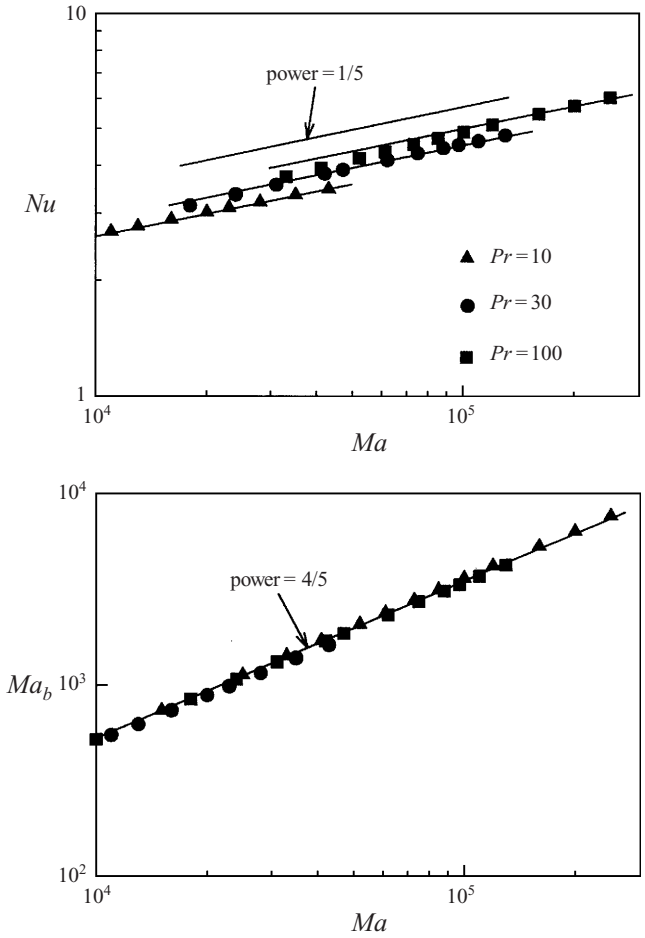

FIGURE 8. Comparison of scaling laws and numerical results.

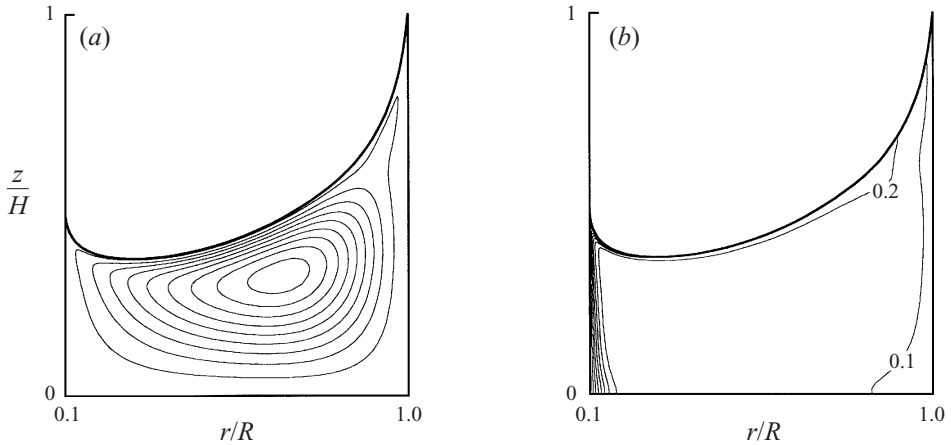

FIGURE 9. Typical streamlines (*a*) and isotherms (*b*) for steady flow with the deep concave free surface ($Ma = 1.9 \times 10^5$, $Pr = 33$, $H_r = 0.1$, $A = 1$, and $V_r = 0.563$).

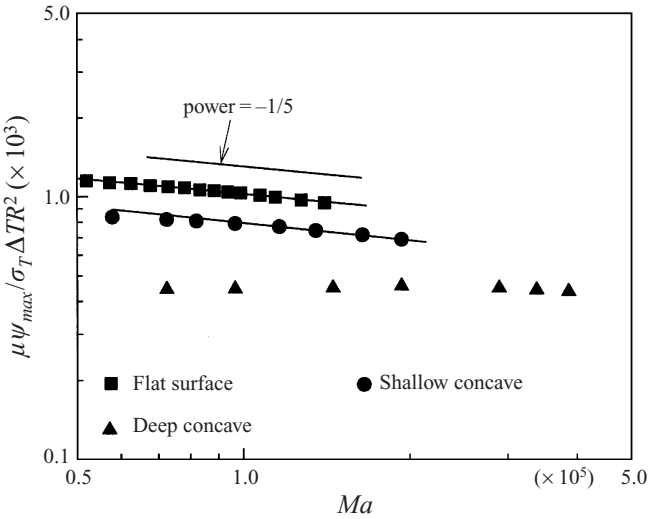

FIGURE 10. Maximum stream function vs. Marangoni number for three free surface shapes ($Pr = 30$, $H_r = 0.1$, $A = 1$).

more concave. The scaling law for ψ_{max} obtained for the flat surface seems to be valid also for the shallow concave surface but not for the deep concave shape.

5. Oscillatory flow with a flat free surface

5.1. *Conditions for onset of oscillations and oscillation frequencies*

It is known from our previous ground-based investigations (Kamotani *et al.* 1992, 1996*b*) that once ΔT is increased beyond a certain value (called ΔT_{cr} herein), the flow field becomes oscillatory and three-dimensional with corresponding time-periodic variations in the temperature field. The transition of steady thermocapillary flow to oscillatory flow was observed in all of the flat and shallow concave surface tests. All of the observed oscillatory flow structures were similar in nature and are sketched in figure 11. In the oscillatory flow, the fluid particles moved back and forth in the azimuthal direction with the frequency of oscillations as they circulated in the flow cell. In addition to the oscillatory motion in the azimuthal direction, a very slow rotation of the whole flow field was also observed. The time period of this rotation was much larger than the time period of the oscillatory motion in the azimuthal direction. In a fixed radial (r, z)-plane, the flow was observed to go through periods of strong and weak motion during one oscillatory cycle. The oscillatory flow structure in microgravity is close to what we found in our normal gravity tests with smaller test sections (Kamotani *et al.* 1992, 1996*b*). A similar flow pattern, slow rotation superposed on main back and forth motion, has also been observed in low-aspect-ratio floating zones (Schwabe, Hintz & Frank 1996).

The values of ΔT_{cr} for onset of oscillations are presented in figure 12 for various test containers. The 1-g data by Kamotani *et al.* (1996*b*) with the same Pr and H_r as in STDCE-2 are also shown. It can be seen that for the test containers with diameter around 1.2 cm, the onset of oscillations in 1-g and microgravity occurs at a similar ΔT_{cr}. A small difference in ΔT_{cr} noticeable in figure 12 is due to different cold wall temperatures in the 1-g ($\sim 25\,^{\circ}$C) and microgravity ($\sim 14\,^{\circ}$C) tests, which resulted in slightly higher viscosity in the microgravity tests for the same fluid. In addition,

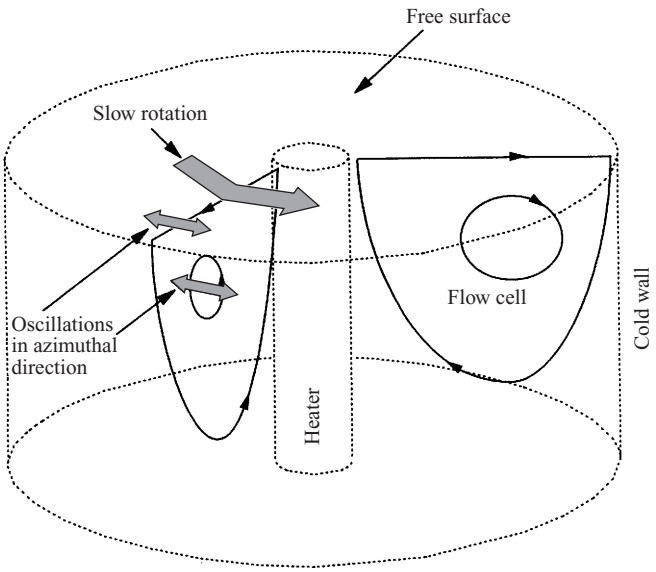

FIGURE 11. Sketch of the oscillatory flow field.

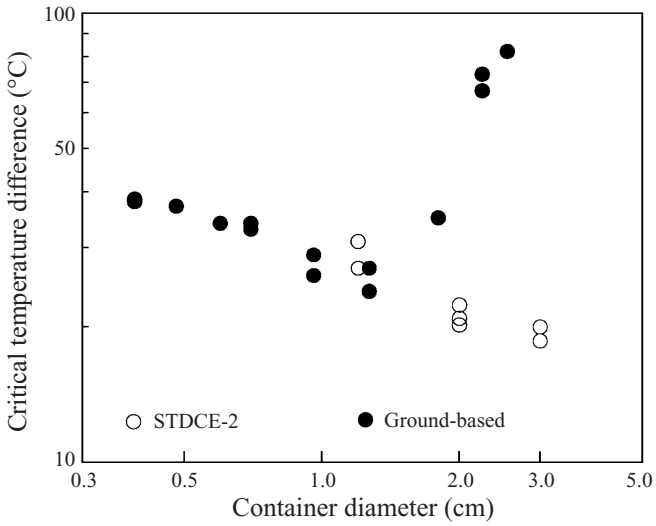

FIGURE 12. Critical temperature differences for onset of oscillations for various sized containers.

for the test containers with approximately 1.2 cm diameter the IR image of the free surface was also similar in the 1-g and microgavity tests. This clearly shows that for the test chambers with 1.2 cm diameter or smaller, buoyancy did not influence the onset of oscillations in our ground-based tests. Based on the 1-g data below 1.2 cm and the microgravity data in figure 12 one can conclude that ΔT_{cr} decreases slightly with increasing test section size in the absence of buoyancy.

One objective of STDCE-2 was to investigate the effect of heater temperature ramp-up rate on the onset of oscillations. It is known that the onset is delayed by ramping-up the heater power too fast. In STDCE-2 this effect was checked by determining the onset of oscillations with different ramping-up rates. In addition to

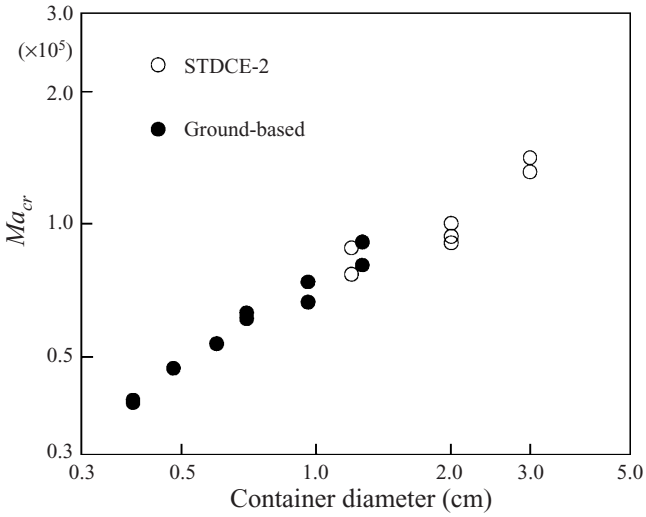

FIGURE 13. Critical Marangoni numbers for various sized containers.

STDCE-2, we performed companion experiments in the Glovebox of USML-2, called OTFE-2, in which oscillatory thermocapillary flow was investigated in cylindrical containers of 1.2 and 2 cm in diameter. The containers were similar to those used in STDCE-2 but with different aspect ratios ($A = 0.5$ and 2). Only flow visualization was employed in OTFE-2. In both STDCE-2 and OTFE-2, as two different ramping-up rates (their difference was 50% to 100%) gave the same critical temperature difference within the experimental error, as in the case of figure 3, we judged the value of ΔT_{cr} to be independent of the ramping-up rate. Only those values are shown in figure 12. OTFE-2 also investigated the effect of ramping-down rate on the disappearance of oscillations. Hysteresis appeared when the heater temperature was decreased too fast. However, when the ramping-down rate was decreased, the difference between ΔT_{cr} for disappearance and that for onset of oscillations became eventually within the experimental error.

In terms of dimensionless parameters, Pr, A and H_r were nearly fixed in all the tests, so the only main parameter varied was Ma. Therefore, the data in figure 12 are non-dimensionalized in terms of Ma_{cr} and plotted in figure 13 against the test container diameter to differentiate among various tests. From figure 13 it is clearly seen that for different tests with similar Pr, A and H_r, the value of Ma_{cr} changes nearly four-fold over the range of the experiments. This shows that Ma_{cr} is not an appropriate parameter to characterize the onset of oscillations. It is clear that some other factor needs to be included. We have obtained the same conclusion concerning the inadequacy of Ma in other configurations also (e.g. Masud *et al.* 1997; Kamotani *et al.* 1998). Our past theoretical and experimental work has shown that free surface deformation plays an important role in the oscillation mechanism. Our concept of oscillations and a new parameter representing free surface deformation will be described later.

The oscillation frequency near the onset of oscillations is shown in figure 14. In the absence of buoyancy the oscillation frequency decreases with increasing test container diameter. The oscillation frequencies measured in our ground-based tests seem to be more sensitive to buoyancy than the onset of oscillations and deviate from the STDCE-2 data trend beyond about $D = 0.9$ cm.

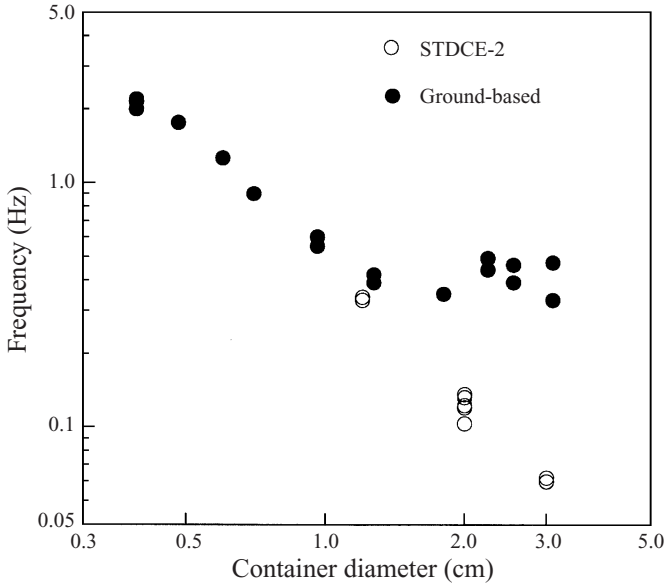

FIGURE 14. Oscillation frequencies near onsets of oscillations for various sized containers.

5.2. *Infrared images and Ronchigrams of the free surface*

Figure 15 shows various isotherm patterns constructed from the IR images observed during oscillations. Figure 15(*a*) shows the pattern observed just after the onset of oscillations in all three test containers. The axial symmetry of the steady-flow IR pattern breaks down into an elliptic (oblong) pattern, called the two-lobed pattern herein, which rotates about the container axis. This pattern suggests that at a given time, convection along the free surface is strong in two diametrically opposed directions indicated by the elongated isotherms, corresponding to the active period in those directions. Similarly, relatively weak convection along the free surface occurs in directions normal to the elongations, corresponding to the slow period in those directions. Therefore, one rotation of the pattern produces two temperature peaks and valleys at a fixed location so that the period of temperature oscillations is one half of the rotational period of the pattern. The IR pattern near the onset of oscillations in our ground-based tests with small containers was also the two-lobed rotating type (Kamotani *et al.* 1996*b*).

For the 1.2 and 2.0 cm test containers, at a higher ΔT, the two-lobed rotating IR pattern changed into the two-lobed pulsating pattern shown in figure 15(*b*). At the start of an oscillation cycle, the elliptic pattern extends radially outward in diametrically opposed directions, and after reaching a peak, it then recedes inwards; subsequently it extends radially outward, again in diametrically opposed directions but this time normal to the first elongations. Thus, the oscillation cycle consists of two pulsations of the two-lobed pattern. The elongations of the isotherms signify stronger convection (active period) similar to the rotating two-lobed pattern discussed earlier. The two-lobed pulsating pattern was not observed for the 3.0 cm test container. Rotating and pulsating patterns were also observed in oscillatory thermocapillary flow in floating zones (Frank & Schwabe 1997).

In the 2.0 and 3.0 cm test containers, at a significantly higher ΔT, the IR oscillation pattern was observed to transition into the three-lobed pulsating pattern shown in

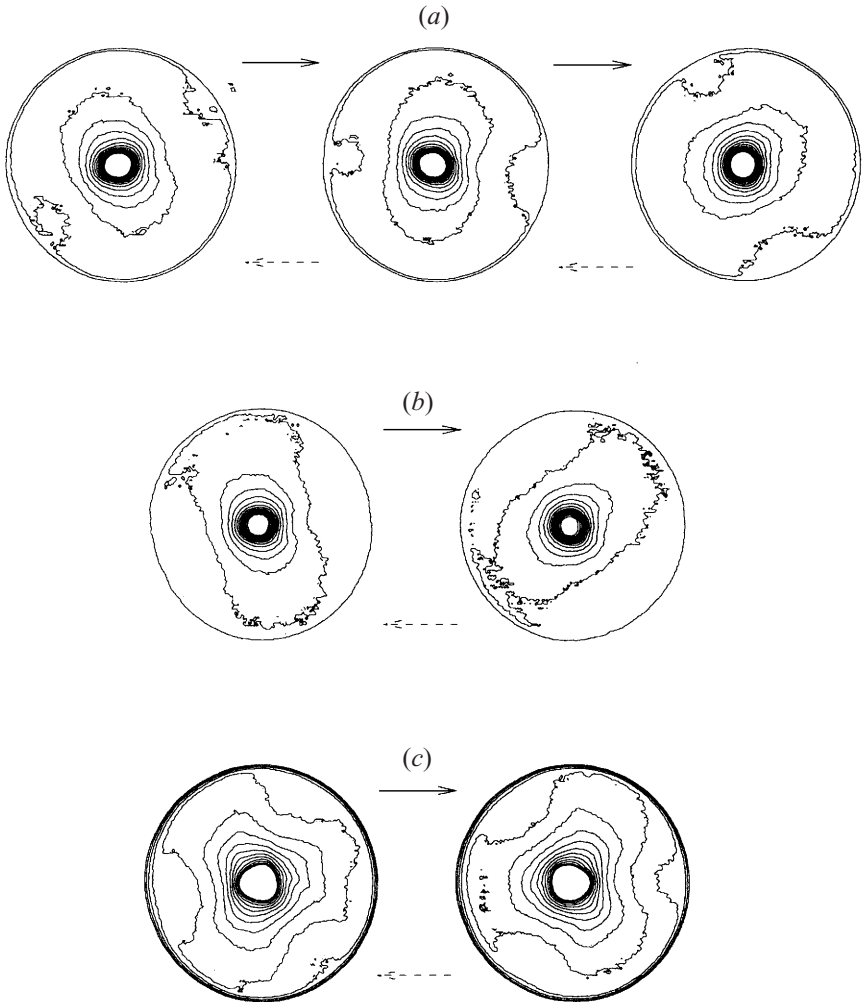

FIGURE 15. Various isotherm patterns measured by the IR imager. (*a*) Two-lobed rotating pattern observed in the range $\Delta T/\Delta T_{cr} < 1.2$ for all diameters. (*b*) Two-lobed pulsating pattern observed at $\Delta T/\Delta T_{cr} = 1.2$ for $D = 1.2$ and 2 cm. (*c*) Three-lobed pulsating pattern observed at $\Delta T/\Delta T_{cr} = 1.4$ for $D = 2$ cm and $\Delta T/\Delta T_{cr} = 1.5$ for $D = 3$ cm.

figure 15(*c*). At the start of an oscillation cycle, the active regions extend radially outward in three equally spaced (azimuthal) directions, and after reaching a peak, these regions recede inwards. Subsequently, the active regions again extend outward in three equally spaced directions but this time these directions are between (azimuthally) the first elongations. Thus, an oscillation cycle consists of two pulsations of the three-lobed IR pattern. The three-lobed pulsating pattern was not observed in the 1.2 cm test container.

The oscillations were also detected by the Ronchi system. However, several factors made accurate measurement of free surface motion difficult. One factor was related to the mean free surface deformation, which was caused by the mean fluid motion and also by the thermal expansion of the test fluid. As with the oscillatory velocity field, the oscillatory component was relatively small compared to the mean part, so when we subtracted the average deformation from the total deformation, the error

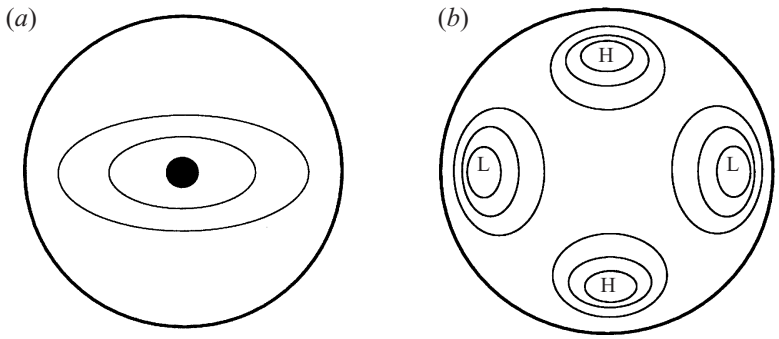

FIGURE 16. Qualitative comparison of (*a*) instantaneous IR image (isotherms) and (*b*) dynamic free surface deformation (contour lines) during oscillations for two-lobe pulsating pattern (H: peak, L: valley).

in the oscillatory deformation measurement became large. The error was especially large near the heater because relatively large surface slope variation occurred there. Another difficulty was that the liquid free surface was constantly subjected to random g-jitter of order approximately 10^{-4} g, where g is the gravitational acceleration on Earth. The amplitude of the associated random free surface waves was generally not very small compared to the deformation due to oscillations. However, the fluid motion induced by g-jitter was mainly sloshing motion, and the lowest natural frequency for the sloshing motion was at least one order of magnitude larger than the thermocapillary oscillation frequencies, so it was possible to differentiate those two motions. Nevertheless, the g-jitter-induced disturbances introduced some errors in the free surface measurement.

By viewing the videotapes of the Ronchigrams, especially in the fast-forward mode, it is very clear that the free surface is in organized wave motion during oscillations. Therefore, the observed dynamic surface motion is described here only qualitatively. As was observed in our ground-based tests (Lin, Kamotani & Ostrach 1995), the most recognizable free surface motion occurred in the region away from the heated region (outside the half-radius point). A typical instantaneous free surface shape is sketched qualitatively in figure 16, which was observed when the IR image showed the pulsating two-lobe pattern. At a given location the surface moved up and down, which was synchronized with the IR image and particle motion. The amplitude of free surface deformation was a few microns near the onset of oscillations and increased to several microns at a higher ΔT. The azimuthal wavenumber of the surface wave was the same as that for the corresponding IR image. The azimuthal direction of a valley (peak) of the surface wave coincided with a high- (low-) temperature direction of the IR image. This indicates that the azimuthal temperature gradients seen in the IR images generate secondary thermocapillary flows from high- to low-temperature regions in the azimuthal direction so that the free surface moves up (down) where temperature is low (high). The back and forth motion of tracer particles sketched in figure 11 is a result of this oscillatory azimuthal flow.

5.3. *Surface deformation parameter*

The physical mechanism of oscillations including free surface deformation has been described for the floating zone configuration (Kamotani & Ostrach 1998) and for the STDCE configuration in the laser heating mode (Kamotani *et al.* 1998). Therefore, only the most important part of the mechanism, namely how the oscillations are

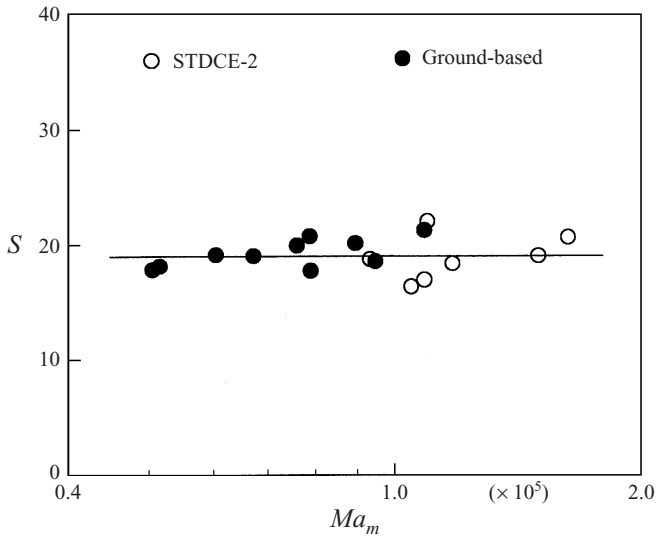

FIGURE 17. Critical S-parameter versus Marangoni number. $Pr_m = 26$–29.

initiated, is discussed here, because it is important for the derivation of a new parameter. The first step occurs in the thermal boundary layer along the free surface in the hot corner. It is a relatively small region but very important for the oscillations because the hot fluid originates there, so if the boundary layer is altered for some reason, the whole temperature field and thus the whole flow field could be affected. Also, when the surface temperature is altered in the hot corner, the adjustment of the return flow is delayed until the free surface is sufficiently deformed to establish a pressure gradient toward the hot corner.

Suppose that the surface velocity is increased in the hot corner during a transient period. Until the bulk flow into the hot corner responds to this change, the surface flow removes the fluid from the region and transports it downstream. Due to the fluid removal from the surface region, cooler fluid is exposed there. As a result, the radial temperature gradient in the hot corner increases, which increases the surface velocity further, so the above process is amplified. The depression of the free surface in the hot corner also reduces the capillary pressure, which then induces fluid motion toward that region and stops the receding of the surface. If the flow is sufficiently altered by the time the surface deformation stops, the active period of surface flow would ensue. After that, the oscillation process is maintained because the temperature field and thus the thermocapillary driving force are continuously altered by the flow. It is noted that the free surface deformation is important only in oscillatory flows and thus can be neglected in the steady flow (as long as the capillary number is small), as was done in the present numerical analysis.

The amount of free surface deformation needed to initiate the oscillations is estimated in the following analysis. We consider the situation near the onset of oscillations, so the velocity and length scales obtained for the basic steady flow can still be used. As in the scaling analysis for the basic flow, A, H_r and Pr are assumed to be fixed, for simplicity. Suppose that the velocity of the surface flow is increased by a certain amount. Since the overall flow is dominated by the bulk flow with velocity scale U_0, we assume that the increased surface velocity scales with U_0. Therefore, the increased surface velocity in the hot corner causes the free surface in that region

to recede with a velocity of order U_0. Suppose also that the free surface in the region deforms by δ_s before the return flow responds and stops the deformation, so that pressure of order $\sigma\delta_s/\delta_{TH}^2$ is generated in region δ_{TH}, which induces a pressure gradient of order $(\sigma\delta_s/\delta_{TH}^2)/R$ in the bulk flow. Due to this pressure gradient, the bulk flow responds to the change in the surface flow after a time lag of order δ_s/U_0 (time of free surface deformation). This response occurs much faster than the viscous diffusion time (R^2/ν) so that the first response is inviscid and thus transient acceleration becomes important (Kamotani *et al.* 1998; Kamotani & Ostrach 1998). Then, the pressure gradient and the acceleration are balanced, namely

$$\rho\frac{U_0}{\delta_s/U_0} \sim \sigma\frac{\delta_s}{\delta_{TH}^2}\frac{1}{R}. \tag{5.1}$$

From (5.1) and (4.8) one obtains

$$\frac{\delta_s}{\delta_{TH}} \sim \left(\frac{\rho U_0^2 R}{\sigma}\right)^{1/2} \sim \left(\frac{\rho\alpha^2}{\sigma R}\right)^{1/2} Ma^{4/5}. \tag{5.2}$$

As sketched in figure 7, the thermal boundary layer thickness along the free surface near the hot corner scales with δ_{TS}. Then, based on the physical model of oscillations, if the ratio δ_s/δ_{TS} becomes finite, the driving force can be significantly modified by the deformation leading to oscillations. Therefore, from (5.2) and (4.7) we define a surface deformation parameter, S, as

$$S = \frac{\delta_s}{\delta_{TS}} = \left(\frac{\rho\alpha^2}{\sigma R}\right)^{1/2} Ma. \tag{5.3}$$

From the above discussion the important condition for the oscillation process to start is that both Ma and S be sufficiently large. Note that, according to (5.3), the only way to distinguish the effect of S and that of Ma on the onset of oscillations for a given fluid is to vary R, as was done in our ground and Space experiments. The critical conditions are plotted in terms of Ma and S in figure 17. Since the onset of oscillations occurs in the hot corner, Ma in figure 17 is based on the viscosity evaluated at the mean fluid temperature in that region, namely $(T_H + T_C)/2$, and designated as Ma_m. Similarly, Pr_m in figure 17 is Pr based on the mean viscosity. As the figure shows, both the ground-based and Space flight data can be correlated well by S: the flow becomes oscillatory when S is larger than about 18. In practice, since the factor $(\rho\alpha^2/\sigma R)^{1/2}$ in (5.3) is generally very small, ranging from 8.8×10^{-5} to 2.4×10^{-4} in our ground and Space experiments, Ma must be large in order to make S larger than about 18 for the onset of oscillations. That is why S alone defines the onset of oscillations in figure 17. The fact that S specifies the onset of oscillations shows that free surface deformation is important in the oscillation phenomenon. The S parameter represents the free surface deformation to initiate the oscillations in the hot corner. The Ronchi system did not have sufficient spatial resolution for hot corner measurements. Besides, a relatively large surface slope variation in that region made the measurement of dynamic free surface motion very difficult, as discussed earlier. Therefore, the Ronchi data could not be used to show the kind of couplings among various quantities that are postulated in the oscillation mechanism. The present work is being continued on the ground to clarify this point.

A question arises as to whether the basic oscillation mechanism involving the organized free surface deformation was affected by the aforementioned g-jitter-induced surface disturbances in the STDCE-2 experiments. The fact that the oscillation process

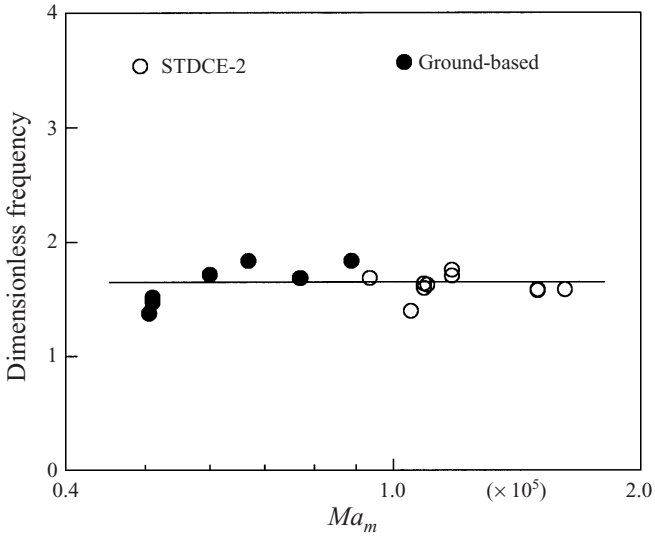

FIGURE 18. Dimensionless oscillation frequencies. $Pr_m = 26$–29.

was observed to be very orderly in many cases shows that the process was not significantly affected by the g-jitter disturbances that are random in nature. Noting that the organized free surface deformation is important for the oscillation mechanism only in the relatively small hot corner, there are some explanations for this lack of strong interference. First, the free surface disturbance frequencies are much smaller than the oscillation frequencies (at least one order of magnitude difference as discussed earlier). Second, the length scale of the sloshing motion caused by g-jitter ($\sim R$) is much larger than the hot corner extent. Third, since the liquid meniscus is anchored at the heater top edge, the free surface near that region is more stable to disturbances.

There are two velocity scales associated with the bulk flow, namely U_0 and V_H. Since V_H is smaller than $U_0(V_H/U_0 \sim Ma^{-2/5})$, the convection time scale R/V_H is larger than R/U_0. Since most of the fluid going into the hot corner passes through the thermal boundary layer along the heater, R/V_H controls the overall convection time there and thus the oscillation period. For that reason, the oscillation frequency (f) is non-dimensionalized by V_H/R, and using (4.8) one obtains the following expression for the dimensionless oscillation frequency (f^*), for a given A and H_r:

$$f^* \equiv \frac{f}{V_H/R} \sim \left(\frac{fR^2}{\alpha}\right) Ma^{-2/5}. \tag{5.4}$$

Since the basic flow scaling law is used in f^*, the above expression is valid only near the onset of oscillations. The dimensionless frequencies measured in STDCE-2 and in our ground-based work with $D \leqslant 0.9$ cm are plotted against Ma_m in figure 18. The dimensionless frequency is nearly constant, equal to about 1.7, in all the tests, showing the appropriateness of the above scaling law.

6. Oscillatory flow under other conditions

A large, highly curved free surface can be obtained only in microgravity, so the present data are quite unique. In the case of a shallow concave free surface, the steady flow was found to transition into a time-dependent three-dimensional flow, similar

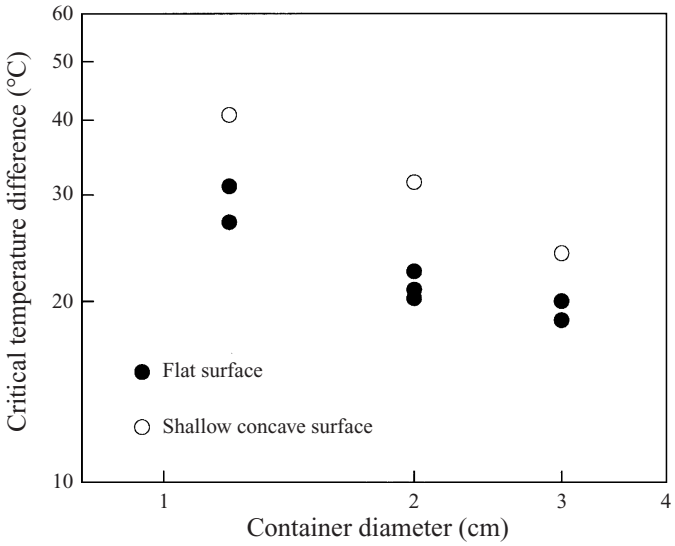

FIGURE 19. Critical temperature differences for flat and shallow concave surface shapes in STDCE-2.

to that found for a flat surface. The critical temperature differences obtained in the shallow concave tests are compared with those in the flat surface tests in figure 19. The values of ΔT_{cr} for the concave are about 30% larger than those for the flat surface. One reason for the increase is that the flow is slower with concave surfaces, as discussed earlier. With deep concave surfaces the flow did not become oscillatory even when the heater power was increased to maximum (which produced ΔT of about 100 °C in each container). In some cases, due to such high heater temperature, bubbles appeared, which made the flow random in space and time, but the transition was clearly due to the bubbles.

In the aforementioned companion experiment, OTFE-2, the effect of A on the onset of oscillations was investigated with flat free surfaces. It was found in OTFE-2 that the critical temperature differences for the shallow containers ($A = 0.5$) were about 50% larger than those found in the corresponding STDCE-2 tests with $A = 1$. The increase is due to the bottom wall effect. Note that the volume ratio for the shallow containers is $V_r = 0.5$, compared to $V_r = 0.56$ for the deep concave shape of STDCE-2. Comparing those V_r values, it seems that the delayed onset of oscillations in the deep concave surface tests cannot be explained by the narrower flow passage alone. As found above, the free surface deformation in the hot corner plays the primary role in the oscillation mechanism. Noting that the free surface is highly curved in the hot corner (see figure 2), the flow and temperature fields and free surface deformation in that region are substantially altered. Exactly how the curved meniscus affects the oscillation mechanism is a complex problem and its analysis is left for future work.

7. Conclusions

Some of the data taken during the STDCE-2 experiments conducted aboard the USML-2 Spacelab in 1995 are presented. Thermocapillary flows were generated in open cylindrical containers filled with a high Prandtl number (~ 30) fluid. The fluid was heated by a cylindrical cartridge heater at the centre. Three test containers with

1.2, 2.0 and 3.0 cm diameters were used. The free surface shape was either flat or concave. Qualitative visualization of the flow field was performed. The entire free surface temperature field was measured with an IR imager. Numerical and scaling analyses were also conducted to obtain useful information on the basic steady flow.

The steady thermocapillary flow was observed to transition to an oscillatory state at a critical temperature difference between the heater and the cold wall. The onset of oscillations in the 1.2 cm diameter test container coincided with the onset of oscillations observed in a comparable test container in our 1-g tests, which shows the negligible influence of buoyancy on the onset of oscillations in this size or smaller containers in normal gravity. The data show that the onset of oscillations measured over a wide range of conditions is not characterized by Ma_{cr}. We then introduce, based on our physical model of oscillations, a new parameter representing the amount of transient free surface deformation relative to the thermal boundary layer thickness in the hot corner, called the S-parameter. The parameter is shown to correlate the experimental onset conditions, determined both in space and on ground, well. The measured oscillation period scales with the time of convection along the heater. The onset of oscillations was delayed when the free surface shape was made increasingly concave and also when the container was made shallow.

The IR images (isotherms) of the free surface during oscillatory flow revealed various oscillatory patterns. Near the onset of oscillatory flow, a two-lobed rotating pattern was observed in all test sections. Subsequent increase in the imposed temperature difference resulted in two-lobed pulsating and three-lobed pulsating patterns. All the oscillatory IR patterns show regions of alternatingly strong and weak convection along the free surface at different stages of an oscillation cycle, which is consistent with our oscillation model. Surface wave were observed during oscillations and they were synchronized with the IR images.

The authors would like to thank many people, especially the NASA Lewis Research Center engineering and operations teams, who worked hard to make STDCE-2 a successful experiment. Special thanks to the payload crew of USML-2, Drs Fred Leslie, Kathy Thornton, Cady Coleman and Al Sacco, who conducted the tests expertly to obtain excellent data. We would like to thank Dr H. Philip Stahl and Mr Kevin Sturtz for designing the Ronchi system and analysing the data. The work done at Case Western Reserve University is supported by NASA under grant NAG3-1568.

REFERENCES

Frank, S. & Schwabe, D. 1997 Temporal and spatial elements of thermocapillary convection in floating zones. *Exps. Fluids* **23**, 234–251.

Kamotani, Y., Chang, A. & Ostrach, S. 1996*a* Effects of heating mode on steady axisymmetric thermocapillary flows in microgravity. *J. Heat Transfer* **118**, 191–197.

Kamotani, Y., Lee, J. H., Ostrach, S. & Pline, A. 1992 An experimental study of oscillatory thermocapillary convection in cylindrical containers. *Phys. Fluids* A **4**, 955–962.

Kamotani, Y., Masud, J. & Pline, A. 1996*b* Oscillatory convection due to combined buoyancy and thermocapillarity. *J. Thermophys. Heat Transfer* **10**, 102–108.

Kamotani, Y. & Ostrach, S. 1998 Theoretical analysis of thermocapillary flow in cylindrical columns of high Prandtl number fluids. *J. Heat Transfer* **120**, 758–764.

Kamotani, Y., Ostrach, S. & Masud, J. 1998 Oscillatory thermocapillary flows in open cylindrical containers induced by CO_2 laser heating. *Intl J. Heat Mass Transfer* **42**, 555–564.

Kamotani, Y., Ostrach, S. & Pline, A. 1994 Analysis of velocity data taken in surface tension driven convection experiment in microgravity. *Phys. Fluids* **6**, 3601–3609.

Kamotani, Y., Ostrach, S. & Pline, A. 1995 A thermocapillary convection experiment in microgravity. *J. Heat Transfer* **117**, 611–618.

Kamotani, Y. & Platt, J. 1992 Effects of free surface shape on combined thermocapillary and natural convection. *J. Thermophys. Heat Transfer* **6**, 721–726.

Lin, J., Kamotani, Y. & Ostrach, S. 1995 An experimental study of free surface deformation in oscillatory thermocapillary flow. *Acta Astronautica* **35**, 525–536.

Malacara, D. 1992 *Optical Shock Testing*. John Wiley & Sons.

Masud, J., Kamotani, Y. & Ostrach, S. 1997 Oscillatory thermocapillary flow in cylindrical columns of high Prandtl number fluids. *J. Thermophys. Heat Transfer* **11**, 105–111.

Pline, A. 1988 Surface temperature measurements for the Surface Tension Driven Convection Experiment. *NASA Tech. Mem.* 101353.

Pline, A. & Butcher, R. 1990 Spacelab qualified infrared imager for microgravity science experiments. *Thermosense XII, SPIE* **1313**, 250–258.

Pline, A., Zurawski, R., Jacobson, T., Kamotani, Y. & Ostrach, S. 1996 Hardware and performance summary of the Surface Tension Driven Convection Experiment-2 aboard the USML-2 Spacelab Mission. Presented at the 47th International Astronautical Congress, Beijing, China, Paper 1AF-96-J.5.01.

Preisser, F., Schwabe, D. & Scharmann, A. 1983 Steady and oscillatory thermocapillary convection in liquid columns with free cylindrical surface. *J. Fluid Mech.* **126**, 545–567.

Schwabe, D., Hintz, P. & Frank, S. 1996 New features of thermocapillary convection in floating zones revealed by tracer particle accumulation structures (PAS). *Microgravity Sci. Tech.* **IX**, 163–168.

Stahl, H. & Stultz, K. 1997 Free surface deformation measurements. *AIAA Paper* 97-0778.

Velten, R., Schwabe, D. & Scharmann, A. 1991 The periodic instability of thermocapillary convection in cylindrical liquid bridges. *Phys. Fluids* A **3**, 267–279.

Wanschura, M., Shevtsova, V. M., Kuhlmann, H. C. & Rath, H. J. 1995 Convective instability mechanisms in thermocapillary liquid bridges. *Phys. Fluids* **7**, 912–925.